ADVANCED FUNCTIONAL MATERIALS
www.afm-journal.de

Eliminating Local Electrolyte Failure Induced by Asynchronous Reaction for High-Loading and Long-Lifespan All-Solid-State Batteries

Hanwen An, Qingsong Liu, Biao Deng, Jian Wang, Menglu Li, Xin Li, Shuaifeng Lou,* and Jiajun Wang**

The design of practical cathodes with high areal capacity in polymer-based all-solid-state batteries remains challenged by the absence of an effective guiding principle that prolongs battery life-span. Unlike liquid batteries, the notorious interface incompatibility between cathodes and electrolytes limited the cycling life of the all-solid-state batteries. Herein, this study proposes a dynamically stable cathode design with a fully covered surface, effectively mitigating interface failure and enabling the cyclic time of batteries with a cathode loading of 12.7 mg cm^{-2} over 10 000 h. This study unveils the importance of local state of charge in affecting the interfacial properties of particles through local oxidative-stability of electrolytes on the interface. This study shows that the phenomena can be strongly influenced by the porosity of the cathode through the perspective of discreteness of ion transport. These insights and approach provide a broader promise for solid batteries for long lifetime.

1. Introduction

All-solid-state lithium batteries (ASSLB).[1] Solid polymer-based batteries are advantageous as low-cost and industrially producible alternatives for future energy storage.[2] As a critical component of the ASSLB, the solid-state composite cathode[3] directly determines the output capacity and energy density. Increasing the loading of the state-of-the-art layered $LiNi_{0.8}Co_{0.1}Mn_{0.1}O_2$(NCM) materials[4] can increase the energy density for practical applications. Unfortunately, there is a notorious adaptability challenge between NCM and conductive polymer electrolyte.[5] Especially in thick composite cathodes, dramatically fast capacity fading[6] rendered NCM unsuitable for polymer batteries.

The conventional studies of capacity fading for the cathodes has focused on the chemical failure due to the inherent instability of electrolyte.[7] Recently, our group found that the state of charge (SOC) inhomogeneity within active particles and loss of structural integrity evoked by local physical contact[8] can eventually lead to the deactivation of sub-particle level domains, while some other study elaborated on the evolution of physical cracks of particle structure induced by the inhomogeneity of its SOC during charging.[9] Nevertheless, the correlation between chemical evolution at the NCM-electrolyte interface and electrode physical structure was disregarded. As a key parameter of solid-state cathode, the contact area between NCM and conductive binder domain (CBD), plays crucial roles on the interface stability of composite cathodes,[3b] yet the structure-activity relationship between contact area and interface stability is still poorly understood. In previous study of high loading cathodes, local micro-architecture was rarely considered. We speculate that it is strongly correlated to ion transport discreteness and capacity fading. Thus, for manufacturing high performance electrodes, a deep understanding of the local structure and charge state of cathode and its interplay with interface evolution is imperatively required.

Here we diagnosed that the oxidative decomposition behavior of electrolytes is correlated with local structure and state of electrode particle. Cathodes with differential contact interface were investigated to demonstrate the inconceivable distinction of chemical evolution at the local contact interface. Porous electrodes with isolated contact surfaces with electrolytes display

H. An, Q. Liu, M. Li, S. Lou, J. Wang
Ministry of Industry and Information Technology (MIIT) Key Laboratory of Critical Materials Technology for New Energy Conversion and Storage
School of Chemistry and Chemical Engineering
Harbin Institute of Technology
Harbin 150001, China
E-mail: shuaifeng.lou@hit.edu.cn; jiajunhit@hit.edu.cn

X. Li
John A Paulson Sch Engn & Appl Sci
Harvard University
Cambridge, MA 02138, USA
E-mail: lixin@seas.harvard.edu

H. An, Q. Liu, S. Lou, J. Wang
Chongqing Research Institute of HIT
Chongqing 401135, P. R. China

B. Deng
Shanghai Institute of Applied Physics
Chinese Academy of Sciences
239 Zhangheng Road, Shanghai 201204, China

J. Wang
Canadian Light Source Inc
University of Saskatchewan
Saskatoon, SK S7N 2V3, Canada

The ORCID identification number(s) for the author(s) of this article can be found under https://doi.org/10.1002/adfm.202305186

DOI: 10.1002/adfm.202305186

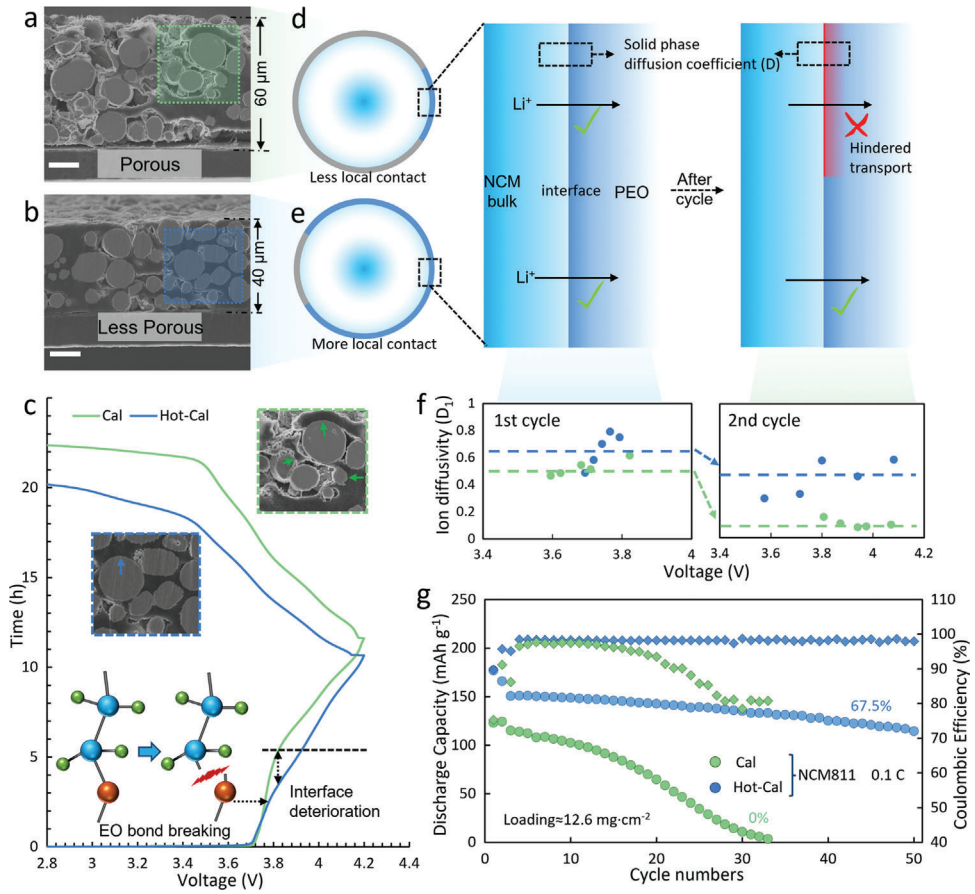

Figure 1. Blocked ion transport in calendaring cathode after cycling. a) Scanning Electron Microscope image of calendaring cathode and b) Hot-calendaring cathode, scale bar 15 μm. c) First charge–discharge curve of the composite cathodes. d) Schematic of ion transport behavior in calendaring cathode and e) Hot-calendaring cathode.f) Comparison of Li-ion diffusion coefficient after the first cycle. g) Cycle performance.

discrete ion transport, which results that the Ni^{4+}-rich region is exposed at the point contact surface of NCM particle with electrolyte. Then the electrolyte was preferentially decomposed into non-conductive interface, a fast capacity fading occurred. In contrast, electrodes with homogeneous contact exhibit homogeneous particle-scale SOC and higher oxidation stability. Hence, a stable interface can be achieved by simultaneously increasing surface coverage by electrolyte and improving the inherent stability of electrolyte. Accordingly, a high-loading composite cathode (12 and 28.6 mg cm^{-2}) with fully active surface was designed via a solvent-free in situ liquid-solid transformation strategy. Benefiting from the dual modification of physical structure remodeling and chemical methods, the design enables high-loading $LiNi_{0.8}Co_{0.1}Mn_{0.1}O_2$ cells to exhibit an excellent lifespan over 10 000 h (500 cycles with retention of 70%). The battery with a cathode loading of 28.6 mg cm^{-2} cycled up to 150 times.

2. Results and Discussion

2.1. Blocked Local Ion Transport in Cathode after Cycling

In solid-polymer cathode (SPC) manufacturing process, the calendaring is also introduced in SPC to increase the contact area between conductive-binder domain (CBD, polymer electrolyte and carbon) and cathode particles for low interface impedance. For ASSLB using polyethylene oxide (PEO) as the electrolyte, hot-calendaring is generally employed to reduce porosity.[10] In this study, polycrystalline $LiNi_{0.8}Co_{0.1}Mn_{0.1}O_2$ (NCM) particles with an average size of 10–20 μm were selected as active materials (Figure S1, Supporting Information). Hence, high-loading composite cathodes with different active surface were prepared by calendaring and hot-calendaring processes, respectively, to explore the evolution discrepancy of interfacial behavior. As shown in **Figure 1**a,b, NCM particles in the calendaring cathode (Cal) were partially covered by CBD, while those in the hot-calendaring cathode (Hot-Cal) were almost fully covered.

The batteries assembled by Cal and Hot-Cal exhibit differences in charge–discharge capacity in Figure 1c. We find that they also show discrepant ion transport rates (Figure S2, Supporting Information) from impedance measurement. This suggests Cal and Hot-Cal may induce different levels of contact inhomogeneity, as illustrated in Figure 1d,e. Correspondingly, the Cal battery displays a transitory voltage plateau at 3.8 V (Figure 1c) likely caused by certain decomposition reactions during the first charge (constant current), which differs from the liquid batteries and Hot-Cal batteries. Previous studies proposed that this phenomenon was highly related to the oxidative instability of PEO-based electrolytes.[7] However, the disappearance of such a

plateau in the charging curve of Hot-Cal batteries with the same composition seems to suggest that PEO is stable at 3.8 V while the issue is at the cathode-electrolyte interface in Cal batteries.

The galvanostatic intermittent titration technique (GITT) was conducted during the initial two charge–discharge.[11] A series of ion diffusivity (D_1) versus voltage in Figure 1f was obtained from GITT data (Figure S3, Supporting Information), in which the D_1 is a normalized diffusion coefficient to describe the ion diffusion rate at the interface (See Experimental Section). Compared to Hot-Cal, a slightly sluggish ion diffusion of Cal may be ascribed to heterogeneous interfacial contact. Nonetheless, the subsequent cycling reaction kinetics of the Cal cathode is more hindered after the first cycle, featured by an obvious drop in ion diffusivity during the second cycle. This phenomenon further supports the schematic depicted in Figure 1d,e, where the CBD on the local contact surface in the Cal cell may be converted to non-conductive phase after the first charging. Furthermore, Hot-Cal cells displayed a lifetime of 50 cycles with a capacity retention of 67.5%, while the Cal cells exhibit significant performance degradation with no capacity after 32 cycles (Figure 1g). The large difference may be closely related to the abnormal voltage plateau at 3.8 V during initial charge–discharge. Overall, the results indicate that the cycling stability of composite cathodes is distinctly dominated by the initial charge–discharge process and local microstructures.

2.2. Quantitative Analysis and Interfacial Local Electrochemical Failure

To obtain more direct information on the correlative behavior between cathode architecture and electro-properties, a quantitative analysis of active surface and interface characteristics is conducted by synchrotron X-ray imaging technology. By adjusting the grey level between NCM and CBD (X-ray absorption of substances is NCM, CBD, Pores), the structure of the interface was reconstructed (shown in **Figure 2**a). As shown in Figure 2b, the virtual slice of the individual components (NCM, CBD and pore) is distinguishable due to their different attenuation to X-rays. Here the direct contact interface between NCM particles and CBD is defined as the active surface (or active area), and the exposed interface to pores with no contact is defined as the inactive surface (Figure 2c). 3D reconstruction imaging displays identical real volume and surface area of the two NCM cathode from Cal cathode and Hot-Cal cathodes (Figure 2d), whereas the Cal cathode show a smaller area of the active surface compared to Hot-Cal cathode (Figure 2e). Considering the same components and similar charge–discharge performance and oxidative stability of these two electrodes, as summarized in Figure 2f, and close NMC and CBD volume (Figure 2g), the obvious increase of battery performance after Hot-Cal is speculated to be caused by the smaller pore volume and the related larger active area, (Figure 2g,h), suggesting that these factors can strongly influence interface reactions of inactive or active areas.

To further investigate charge transfer reactions at cathode interfaces, in situ Fourier transform infrared spectroscopy (FTIR, absorption mode) was performed to track the idiographic chemical variation (the in situ FTIR cell structure is shown in Figure S4, Supporting Information). As the Potential-Wavenumber graphics of Cal batteries in **Figure 3**a, the absorption peaks at 1200, 1275, and 1320 cm^{-1} appear when the charging voltage reaches about 3.8 V, which correspond to the oxidation impurities of PEO-based electrolyte, CF_3-R, CF_3-SO_2-O-CH_2-R, and SO_2-R.[12] Contrary to Cal batteries, no obvious oxidative decomposition product in the Hot-Cal batteries was observed (Figure 3b,c,d).

The continuous deterioration of PEO can trigger the formation of non-conductive interface on the active area in Cal batteries (Figure 3e), and an incremental interfacial resistance with battery charging. Hence, we conducted in situ electrochemical impedance spectroscopy (EIS) test to evaluate the ion transport kinetics at different charging voltages. As the EIS presented in Figure 3f, the two electrodes exhibit similar values of membrane impedances before charging, and the slight difference could be ascribed to the variant thickness of the electrolyte membrane. In the mid-frequency range of EIS in ASSLB, the diameter of the semicircular arc is considered to be the interface impedance.[13] Owing to the more discontinuous contact, Cal batteries exhibits a higher initial interfacial impedance compared to Hot-Cal. With charging, the Cal batteries showed a continuous interfacial impedance growth, which is consistent with the decomposition of electrolyte as detected by our FTIR. On the contrary, no significant increase of impedance in Hot-Cal electrode was observed. Previous research suggested that the cycling degradation is related to the oxidation instability of PEO, while our results here demonstrate that a proper design of cathode microstructure by Hot-Cal can mitigate the degradation, which seems to question the assumption that such decomposition is caused by the voltage instability of PEO.

To gain more explicit insights into the degradation mechanisms of the Cal batteries, we employed a confocal Raman system to characterize the particle-scale SOC. The phase transition of the active material NCM could be estimated by the intensity ratio of Eg/A1g in Raman spectroscopy, where higher Eg/A1g ratio can indicate more higher SOC of the NCM particle.[14] For the Cal cathode before cycle, both good and poor contact particle (Figure S5, Supporting Information) feature very close ratio of E_g/A_{1g}, as the Raman spectroscopy shown in Figure 3g,h. The poor-contact particles demonstrate an increase of E_g/A_{1g} while the good-contact particles have the same ratio after 20 cycles (Figure 3h). The phenomena suggests that poor-contact particles in Cal are more prone to increased SOC after cycling, most probably caused by blocked Li^+ intercalation in discharge. Combined with the results of electrolyte deterioration confirmed by FTIR for the cathode region in the Cal cell, we deduce that the electrolyte is decomposed at the active area of poor-contact particles due to the higher local SOC.

2.3. Electrolyte Failure Induced by Local Region of High Delithiation State

Delithiation reactions (Ni^{3+} to Ni^{4+}) in solid-state batteries rely on Li^+ transport through the active surface during charging, the NCM particle of Cal batteries with both inactive and active areas (**Figure 4**a,c) reacts preferentially on the active surface due to the isolated ion transport.[6a] Consequently, a Li^+ concentration gradient at the particle scale was formed at the same elec-

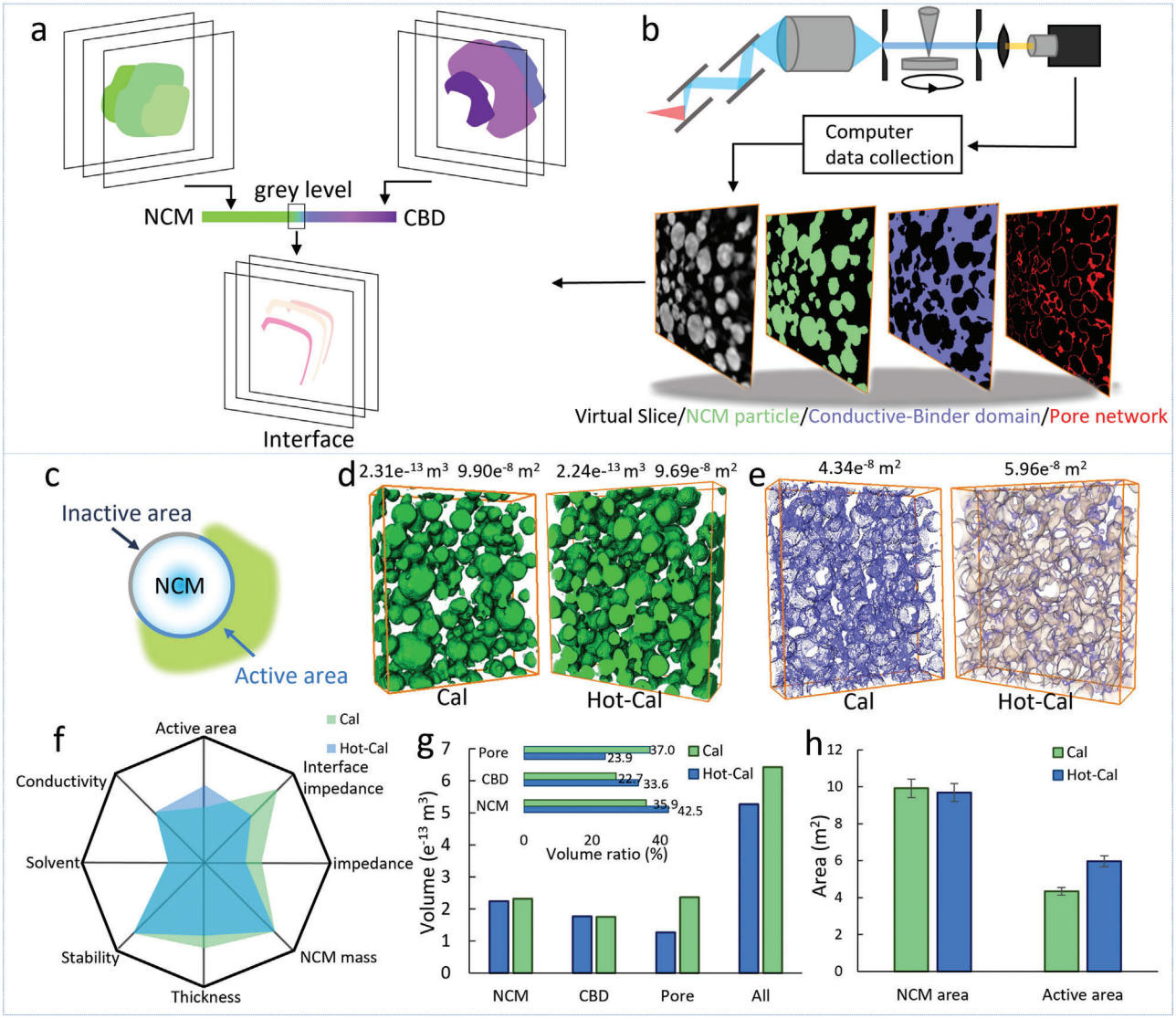

Figure 2. Quantitative analysis of the active area of Cal cathodes and Hot-Cal cathodes. a) The principle of reconstructing interface from grey level. b) Synchrotron X-ray tomography virtual slice and corresponding phase of the cathode. c) Schematic of inactive/active surface. d) 3D microstructure of NCM and e) active area shown by tomography reconstruction with volume rendering, the viewport size of all presentation structures is 200 × 200 μm^2. f) Comparison of physicochemical parameters of cathodes (Solvent: Residual acetonitrile solvent in electrolyte, Thickness: Electrode thickness; Conductivity: Ionic conductivity of CBD). g) The volume ratio of each phase based on synchrotron X-ray tomography. h) The proportion of active area on the NCM surface.

trode potential (or degree of delithiation), indicating a higher Ni^{4+} concentration at the active surface (Figure 4e). In contrast, NCM is more evenly wrapped (Figure 4b,d) in Hot-Cal cells, inducing a more homogeneous distribution of Ni^{4+} at the particle level (Figure 4f), and thus less local Ni^{4+} concentration at a given SOC. This can cause drastic differences in the electrochemical stability at local interfaces. For example, transition metal (TM) elements with high valence may play a role in accelerating the catalytic decomposition of organic electrolytes (Figure 4g).[7a,15] Using interface stability calculation based on the standard pseudo-binary approach,[16] the interface reaction between electrolyte and NCM is calculated (Figure S6, Supporting Information) with the interface reaction energy presented in Figure 4h. With the increase in the degree of delithiation, the energy gradually decreases, indicating a higher reactivity between the PEO-based electrolyte and Ni^{4+} on the NCM surface.

Moreover, confocal Raman spectroscopy was carried out again to further investigate electrolyte degradation inside Cal electrodes, in light of the comparative analysis shown in Figure 4i,j. The band at 734 cm^{-1}, a response of interaction between $TFSI^-$ and TM, shifted and disappeared after cycling for poor-contact particles.[17] This demonstrates that the interaction between LiTFSI and NCM disappears, and LiTFSI decomposes, resulting in a series of deterioration effects of the electrolyte. However, the signal of interaction for good-contact particles are still visible after cycling. By comparing the above results, the discrepant Ni^{4+}/Ni^{3+} ratios caused by the inhomogeneity of Li^+ transport may be the key factor leading to the interface failure.

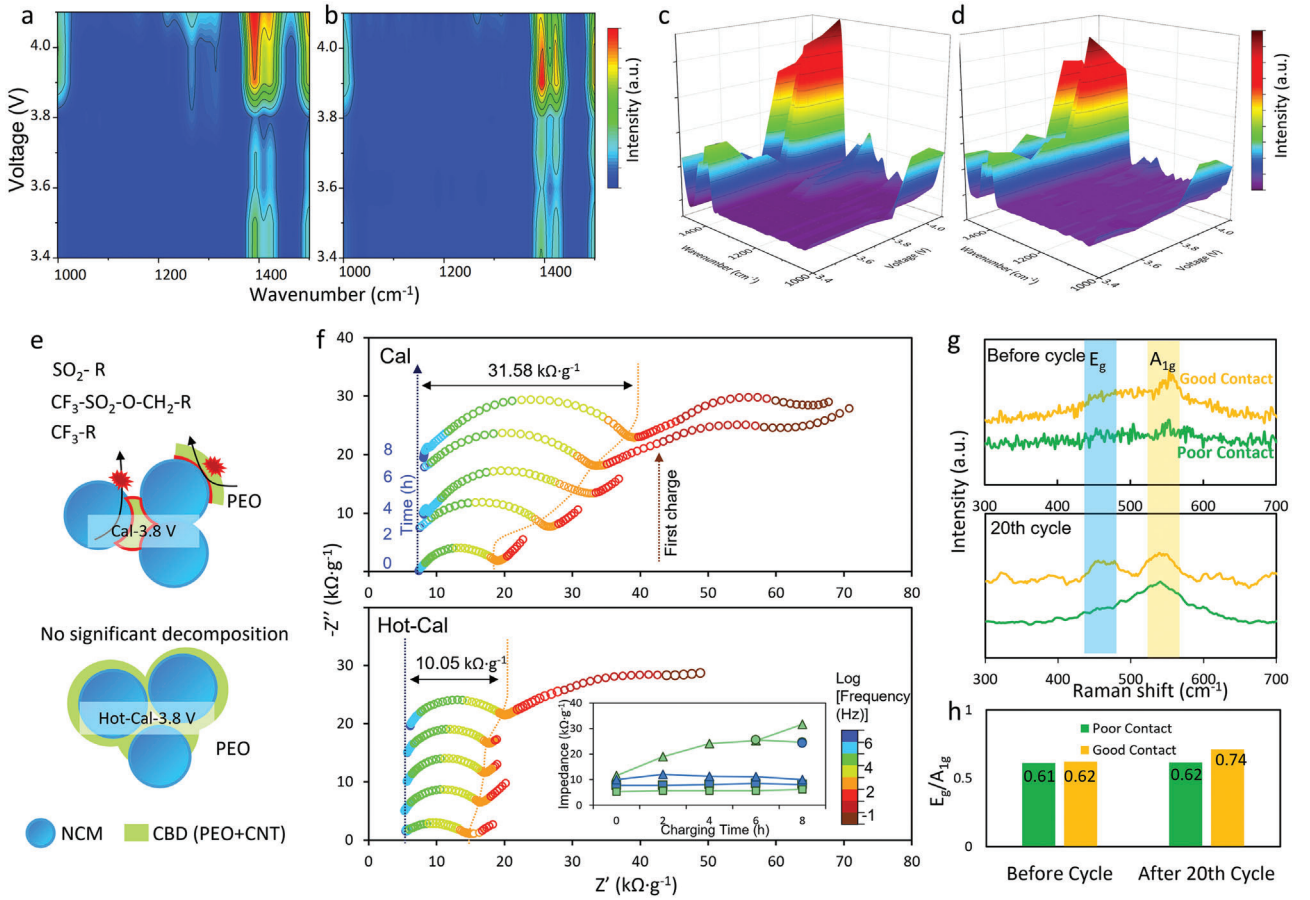

Figure 3. Interfacial chemical failure of the Cal cathodes with local ion transport. a) In situ FITR spectrum of calendaring cathode and b) Hot-calendaring cathode. c) 3D FITR of calendaring cathode and d) Hot-calendaring cathode. e) Schematic of local chemical failure on NCM particle during charging. f) Comparison of interface impedance evolution during first charging, as well as the image of poor contact and good contact particle. g) Raman spectrum of particles before and after cycling. h) Comparison of intensity ration of E_g/A_{1g}.

To further validate the formation of the local region with a high ratio of Ni^{4+}/Ni^{3+}, synchrotron scanning transmission X-ray microscopy (STXM) was employed to reveal the local distribution of Ni element in the two cathodes (Cal and Hot Cal). The STXM can provide high-resolution soft X-ray absorption spectroscopy (XAS) of 2D spatial distribution.[18] As shown in Figures 4k–n, the ptychography of the Cal cathode (Figure 4k) reveals that region 1 and 2 exhibits a higher X-ray absorption degree than that in the regions 3 and 4 due to the high concentration of Ni^{4+}. Moreover, Figure 4m draws the Ni^{4+} rich areas (red) corresponding to region 1 and 2, and rich Ni^{3+} areas (green) corresponding to region 3 and 4. By contrast, the ptychography of the Hot-Cal cathode (Figure 4l,n) displays a uniform phase distribution, which can be confirmed by the corresponding XAS spectra of Ni L-edge at different regions (Figure 4o,p). For the particle of Cal cathode, region 1 shows a high-intensity ratio of Ni^{4+}/Ni^{3+} (1.37), but region 4 shows a low ratio of 0.75. In contrast, the particle of Hot-Cal illustrates a relatively average ratio of Ni^{4+}/Ni^{3+} (0.97≈1.07). The intensity ratio of Ni^{4+}/Ni^{3+} of the particle in Cal is downgraded along the direction of regions 1 to 4, and the ratio of region-1 in Cal batteries is higher than the ratio of any region of the particle in Hot-Cal (Figure 4q).

By combining the theoretical calculation, we conclude that the local contact leads to a Ni^{4+}-rich region at the interface during charging for the cathode with the heterogeneous inner physical contact of ASSLB. Therefore, the SOC of local contact region is higher than the apparent SOC of the overall electrode, which is asynchronous charge equilibration effects. The generation of a high concentration of Ni^{4+} promotes interfacial reactivity and exacerbates the decomposition of organic electrolytes. This also explains that the actual working potential of PEO is much lower than the electrochemical oxidation stability window under Linear Sweep Voltammetry (LSV) test (Figure 4r).

2.4. Dynamically Stable Design for Long Life Batteries

To avoid unfavorable inactive surface during solvent evaporation (Figure S7a, Supporting Information), the solvent-free method seems to be more suitable for the preparation of polymer-based solid-state composite electrodes.[19] Besides, adopting an interfacial modification strategy is necessary to improve the compatibility considering the intrinsic chemical stability of PEO and NCM. Both the active area and intrinsic electrochemical stability need to

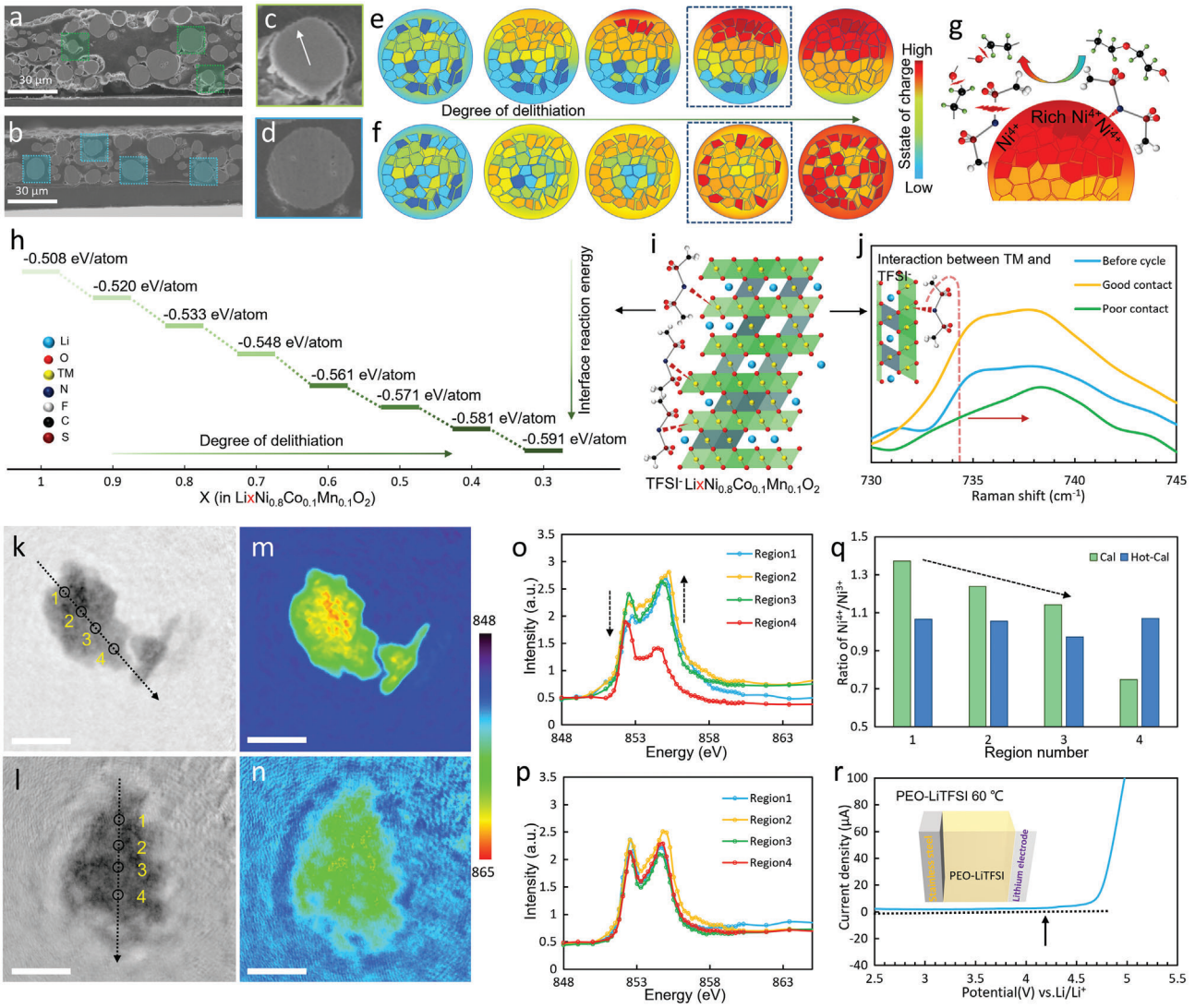

Figure 4. High state of charge in particle scale at local contact accelerates the decomposition of electrolyte. a) Scanning Electron Microscope image of calendaring cathode and b) Hot-calendaring cathode, scale bar 30 μm, and the c) local contact NCM particle, d) evenly wrapped particle. e) Schematic of SOC distribution during charging corresponding to local contact NCM particle and (f) evenly wrapped particle. g)The decomposition of electrolyte on the surface with a high concentration of Ni^{4+}. h) Interface reaction energy between $Li_xNi_{0.8}Co_{0.1}Mn_{0.1}O_2$ and $TFSI^-$. i) Adsorption of $TFSI^-$ and transition metal elements. j) Raman spectrum of particles before and after cycling. k) Ptychography STXM amplitude (optical density) image of the particle in calendaring batteries and l) Hot-calendaring cathode, disassembled from the full cell at the stable voltage of 4 V, the viewport size is 2.5 × 2.5 μm^2. m) Elemental distribution mapping at the Ni edges of NCM particle in Cal batteries and n) Hot-Cal batteries. o) XAS spectra of Ni L3-edge in different regions extracted from Figure 4m) and pfrom Figure 4n. q) Quantification of the Ni^{4+}/Ni^{3+} intensity ratio along region-1 to region-4. r) Linear sweep voltammetry of PEO-LiTFSI.

be considered for solid-state battery matching high-voltage positive electrode, and this strategy also has certain guiding significance for inorganic solid-state battery.

Herein, the cathode with a fully active surface is designed by an in situ liquid-solid transformation approach to prevent asynchronous charge equilibration. Specifically, in the cathode slurry compounding process, a solvent-free and liquid ion-conductive mixture, containing PEO derivatives (poly(ethylene glycol)diacrylate, PEGDA), nitrile-based additives (ethyl cyanoacrylate, ECA) and Li salt, was used as dispersants to obtain uniform cathode slurries (Figures S7b and S8, Supporting Information). The liquid is then transformed into a conductive polymer in homogeneous and intimate contact with the NCM via in situ thermal polymerization. Meanwhile, nitrile-based additive as interpolymer is used to stabilize the NCM-electrolyte interface. This "two-pronged" approach enables homogeneous interfacial ion transport and high-voltage interfacial stability inside the polymer-based solid-state composite cathode.

FTIR was conducted to confirm the interaction between NCM and poly(ethyl cyanoacrylate) (PECA). In Figure S9, Supporting Information, the disappeared peak of the —C≡N group at 2252 cm^{-1} indicates the adsorption of PECA on NCM. The adsorption sites of the Ni atom are occupied by the —C≡N group that replaces the $TFSI^-$, which stabilize the interface due to the remission of

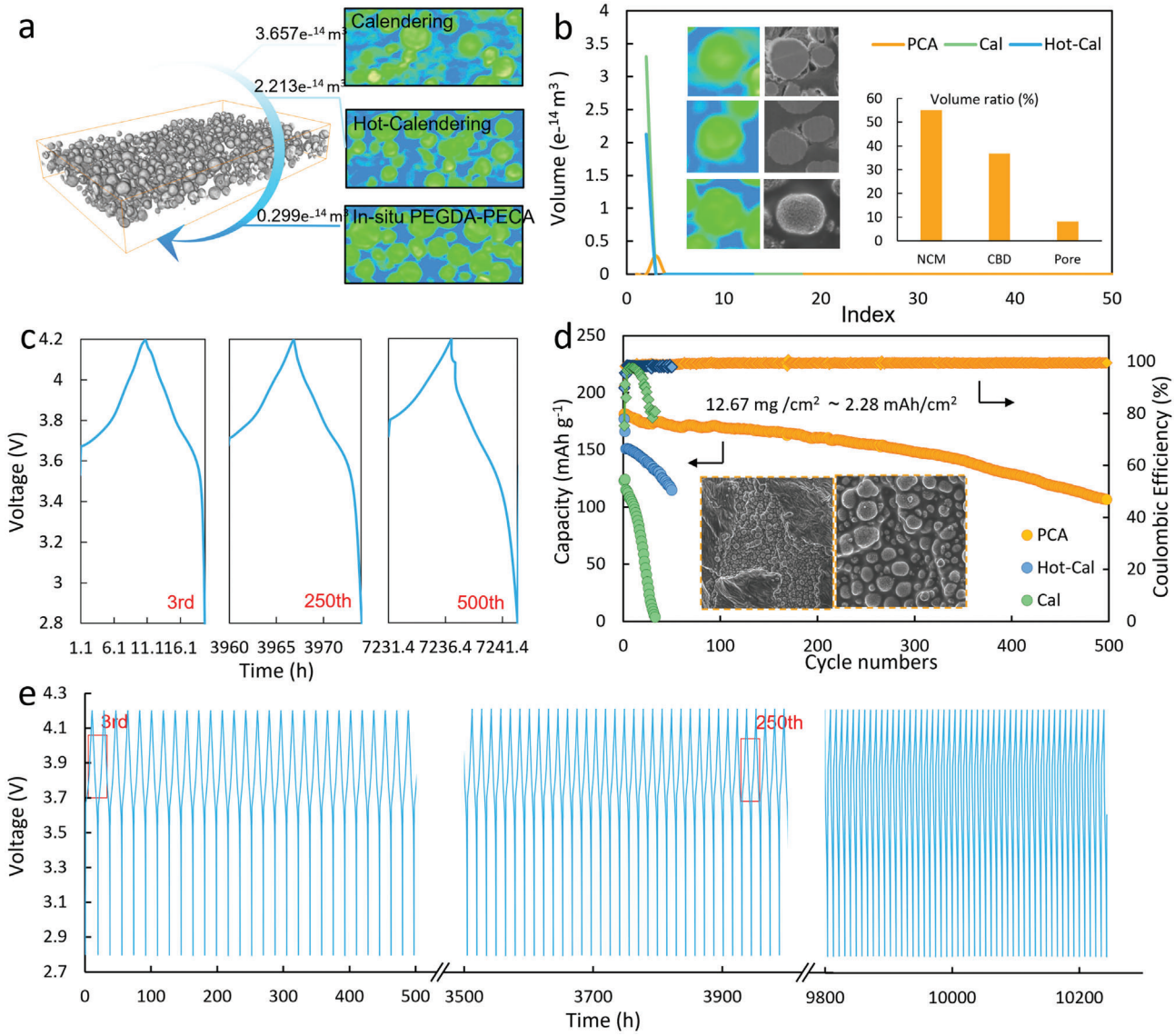

Figure 5. Fully active surface design for stable interface and battery performance. a) 3D reconstruction of PCA and slice of Cal, Hot-Cal, and PCA. b) Index-volume curve extracted from the 3D reconstruction of different cathodes. c)The 3rd, 250th, 500th time-voltage curve of PCA. d) Cyclic performance of ASSLBs with Cal, Hot-Cal, and PCA cathode, and the surface morphology of PCA, scale bar, 100 µm, 30 µm. e) Time-voltage curve of PCA.

$TFSI^-$ decomposition.[20] The high stability of ECA on the surface of NCM is verified by the calculated interfacial reaction energies (Figure S10, Supporting Information). Furthermore, the long cycle life can benefit from the high electrochemical window (>5.3 V, Figure S11a, Supporting Information) and fast conductivity (0.43 mS cm^{-1}, Figure S11b,c, Supporting Information) of the copolymer poly(ethylene glycol)diacrylate-poly(ethyl cyanoacrylate) (PEGDA-PECA), and the battery showed excellent discharge capacity at 30–100 °C (Figure S11d, Supporting Information). Besides, a copolymer containing a mass fraction of 5% ECA is selected as the CBD base because of its good electrical conductivity and oxidation resistance (Figure S11e, Supporting Information).

Importantly, the NCM particles in the composite cathode PEGDA-PECA-NCM (PCA) are homogeneously wrapped and intimately contacted with the conductive-binder domain (Figure S12, Supporting Information). The synchrotron X-ray imaging (**Figure 5**a,b) shows an extremely lower pore volume of PCA cathode (0.30×10^{-14} m^3), in contrast to both Cal cathode (3.65×10^{-14} m^3) and Hot-Cal cathode (2.21×10^{-14} m^3), which means an even SOC of each particle during charging can be expected. Although the decomposition of electrolytes at the interface is inevitable, dynamic stability can be achieved by tailoring fully active surface cathode.

Consequently, an impressive long cyclic life over 500 cycles with an ultra-high loading of 12.7 mg cm^{-2} (0.1 C) is demonstrated in the full cell assembled by $LiNi_{0.8}Co_{0.1}Mn_{0.1}O_2$ as active materials, PEO-$Li_{6.4}La_3Zr_{1.4}Ta_{0.6}O_{12}$ as electrolyte membrane (Figure 5c,d and Figure S12c,d, Supporting Information). It is noteworthy that the charge and discharge curves were flat and

the voltage polarization remained small after long cycles (Figures S12e,f and S13a, Supporting Information). This ultra-long cyclic time (over 10 000 h, Figure 5e, Figure S13b, Supporting Information) provides strong evidence for the oxidation resistance of PCA cathodes. In addition, higher loading (28.6 mg cm^{-2}) of PCA batteries exhibited discharge specific capacity of more than 160 mAh g^{-1} (4.85 mAh cm^{-2}) at 0.2 C, cycled up to 150 cycles (retention of 77.9%, Figure S14a, Supporting Information). The cyclic performance of the dual-modified cathode is better than that of the single-modified cathode (PEGDA cathode: homogeneous contact but insufficient oxidation stability; and PEO-CAN: high oxidation resistance but insufficient active area, Figure S14b, Supporting Information). Figure S15, Supporting Information, showed the unprecedented performance of this work relative to the reported PEO high voltage batteries.[7a,b,12,21] These results suggest that devising the electrode with the fully active surface is a promising route enabling high-energy-density ASSLB in practical industrial applications.

3. Conclusion

In summary, we revealed the unique correlation between local microstructure and interfacial chemical stability in solid-state cathodes. Overall results demonstrate that the actual electrochemical oxidation-resistance stability of the electrolyte is severely affected by the local structure and charge state inside the solid-state electrode. The localized transport results in severe inhomogeneity of particle-scale SOC and asynchronous charge equilibration. Thereby a continuous degradation of the conductive-binder domain is exacerbated by high-valence transition metals on the local surface of active materials, leading to irreversible capacity loss and reduced cycle life. After manipulating the area of the active surface and improving the electrochemical window of the electrolyte to achieve a kinetically stable interface, excellent charge–discharge time over 10 000 h of the composite cathode with 12.7 mg cm^{-2} loading was obtained, and the cathode with higher areal capacity (28.6 mg cm^{-2}, 4.85 mAh cm^{-2}) also exhibits a cycle life over 150 cycles. Our study provided both insights into the degradation mechanism of electrolytes and a promising route to develop high-energy-density ASSLB.

4. Experimental Section

All experimental details are included in the Supporting Information.

Supporting Information

Supporting Information is available from the Wiley Online Library or from the author.

Acknowledgements

This work was supported by the National Natural Science Foundation of China (No. 22075063, No. U1932205), Chinesisch-Deutsches Mobilitätspropgamm (M-0281), the Fundamental Research Funds for the Central Universities (No. HIT.OCEF.2021028), Natural Science Funds of Heilongjiang Province (No. ZD2019B001), Heilongjiang Touyan Team (No. HITTY-20190033), the Natural Science Fund for Distinguished Young Scholars of Chongqing (cstc2021jcyj-jqX0003), "Young Scientist Studio" of Harbin Institute of Technology (HIT), and funds from Chongqing Research Institute of HIT. This research used resources at the Canadian Light Source, a national research facility of the University of Saskatchewan, which is supported by the Canada Foundation for Innovation (CFI), the Natural Sciences and Engineering Research Council (NSERC), the National Research Council (NRC), the Canadian Institutes of Health Research (CIHR), the Government of Saskatchewan, and the University of Saskatchewan. The authors thank the beamline BL13W1 and BL18B at Shanghai Synchrotron Radiation Facility (SSRF) for SR-CT measurements, and 4W1A beamline of Beijing Synchrotron Radiation Facility (BSRF).

Conflict of Interest

The authors declare no conflict of interest.

Data Availability Statement

The data that support the findings of this study are available from the corresponding author upon reasonable request.

Keywords

asynchronous charge-equilibration, electrochemical stability, high-loading cathodes, solid-state batteries, synchrotron techniques

Received: May 10, 2023
Revised: June 11, 2023
Published online:

[1] a) L. Ye, X. Li, *Nature* **2021**, *593*, 218; b) S. Randau, D. A. Weber, O. Kötz, R. Koerver, P. Braun, A. Weber, E. Ivers-Tiffée, T. Adermann, J. Kulisch, W. G. Zeier, F. H. Richter, J. Janek, *Nat. Energy* **2020**, *5*, 259; c) Y. Lu, Z. Tu, L. A. Archer, *Nat. Mater.* **2014**, *13*, 961; d) Z. Hou, J. Zhang, W. Wang, Q. Chen, B. Li, C. Li, *J. Energy Chem.* **2020**, *45*, 7; e) S. Lou, F. Zhang, C. Fu, M. Chen, Y. Ma, G. Yin, J. Wang, *Adv. Mater.* **2021**, *33*, 2000721; f) Z. Yu, X. Zhang, C. Fu, H. Wang, M. Chen, G. Yin, H. Huo, J. Wang, *Adv. Energy Mater.* **2021**, *11*, 2003250; g) H. Wang, H. An, H. Shan, L. Zhao, J. Wang, *Acta Phys. Chim. Sin.* **2020**, *0*, 2007070.

[2] a) M. J. Lee, J. Han, K. Lee, Y. J. Lee, B. G. Kim, K. N. Jung, B. J. Kim, S. W. Lee, *Nature* **2022**, *601*, 217; b) C. Yang, Q. Wu, W. Xie, X. Zhang, A. Brozena, J. Zheng, M. N. Garaga, B. H. Ko, Y. Mao, S. He, Y. Gao, P. Wang, M. Tyagi, F. Jiao, R. Briber, P. Albertus, C. Wang, S. Greenbaum, Y. Y. Hu, A. Isogai, M. Winter, K. Xu, Y. Qi, L. Hu, *Nature* **2021**, *598*, 590; c) L. L.-l. PAN Xiao-na, W. A. N. G. Zhi-pu, W. A. N. G. Dan, L. I. Yun, Y. A. N. G. Pei-xia, Z. H. A. N. G. Jin-qiu, A. N. Mao-zhong, *J. Electrochem.* **2020**, *26*, 406; d) Z.-l. G. Xue Li, *J. Electrochem.* **2020**, *26*, 338; e) W.-Q. Wei, B.-Q. Liu, Y.-Q. Gan, H.-J. Ma, D.-W. Cui, *Rare Met.* **2020**, *40*, 409; f) L. Dong, S. Zhong, B. Yuan, Y. Li, J. Liu, Y. Ji, D. Chen, Y. Liu, C. Yang, J. Han, W. He, *Angew. Chem., Int. Ed. Engl.* **2023**, *62*, 202301073.

[3] a) X. Yang, K. Doyle-Davis, X. Gao, X. Sun, *eTransportation* **2022**, *11*, 100152; b) X. Lu, S. R. Daemi, A. Bertei, M. D. R. Kok, K. B. O'Regan, L. Rasha, J. Park, G. Hinds, E. Kendrick, D. J. L. Brett, P. R. Shearing, *Joule* **2020**, *4*, 2746; c) X. Judez, G. G. Eshetu, C. Li, L. M. Rodriguez-Martinez, H. Zhang, M. Armand, *Joule* **2018**, *2*, 2208; d) R. Zhang, Y. Dong, M. A. Al-Tahan, Y. Zhang, R. Wei, Y. Ma, C. Yang, J. Zhang, *J. Energy Chem.* **2021**, *60*, 85; e) C.-L. Yan, *Rare Met.* **2020**, *39*, 458.

[4] a) Z. Wang, X. Li, Y. Chen, K. Pei, Y.-W. Mai, S. Zhang, J. Li, *Chem* **2020**, *6*, 2878; b) H. Yu, Y. Cao, L. Chen, Y. Hu, X. Duan, S. Dai, C. Li, H. Jiang, *Nat. Commun.* **2021**, *12*, 4564; c) L. Wang, A. Dai, W. Xu, S. Lee, W. Cha, R. Harder, T. Liu, Y. Ren, G. Yin, P. Zuo, J. Wang, J. Lu, J. Wang, *J. Am. Chem. Soc.* **2020**, *142*, 14966.

[5] Q. Zhao, P. Chen, S. Li, X. Liu, L. A. Archer, *J. Mater. Chem. A* **2019**, *7*, 7823.

[6] a) S. Lou, Q. Liu, F. Zhang, Q. Liu, Z. Yu, T. Mu, Y. Zhao, J. Borovilas, Y. Chen, M. Ge, X. Xiao, W. K. Lee, G. Yin, Y. Yang, X. Sun, J. Wang, *Nat. Commun.* **2020**, *11*, 5700; b) Y. J. S. Xue Sun, R. L. Li, *Jia-Jun Wang* **2022**, *28*, 2214011; c) X. S. Ya-Jie Song, L.i-P. Ren, L. Zhao, F. P. Kong, J. J. Wang, **2022**, *28*, 2108461.

[7] a) X. Wang, Y. Song, X. Jiang, Q. Liu, J. Dong, J. Wang, X. Zhou, B. Li, G. Yin, Z. Jiang, J. Wang, *Adv. Funct. Mater.* **2022**, *32*, 2206976; b) J. Qiu, X. Liu, R. Chen, Q. Li, Y. Wang, P. Chen, L. Gan, S. J. Lee, D. Nordlund, Y. Liu, X. Yu, X. Bai, H. Li, L. Chen, *Adv. Funct. Mater.* **2020**, *30*, 1909392; c) M. Nakayama, S. Wada, S. Kuroki, M. Nogami, *Energy Environ. Sci.* **2010**, *3*, 1995.

[8] M. M. Besli, S. Xia, S. Kuppan, Y. Huang, M. Metzger, A. K. Shukla, G. Schneider, S. Hellstrom, J. Christensen, M. M. Doeff, Y. Liu, *Chem. Mater.* **2018**, *31*, 491.

[9] X. Lu, A. Bertei, D. P. Finegan, C. Tan, S. R. Daemi, J. S. Weaving, K. B. O'Regan, T. M. M. Heenan, G. Hinds, E. Kendrick, D. J. L. Brett, P. R. Shearing, *Nat. Commun.* **2020**, *11*, 2079.

[10] R. J. Chen, Y. B. Zhang, T. Liu, B. Q. Xu, Y. H. Lin, C. W. Nan, Y. Shen, *ACS Appl. Mater. Interfaces* **2017**, *9*, 9654.

[11] J. Wang, L. Wang, C. Eng, J. Wang, *Adv. Energy Mater.* **2017**, *7*, 1700544.

[12] C. Fu, S. Lou, X. Xu, C. Cui, C. Li, P. Zuo, Y. Ma, G. Yin, Y. Gao, *Chem. Eng. J.* **2020**, *392*, 123665.

[13] B. Zahiri, A. Patra, C. Kiggins, A. X. B. Yong, E. Ertekin, J. B. Cook, P. V. Braun, *Nat. Mater.* **2021**, *20*, 1392.

[14] H. Cha, J. Kim, H. Lee, N. Kim, J. Hwang, J. Sung, M. Yoon, K. Kim, J. Cho, *Adv. Mater.* **2020**, *32*, 2003040.

[15] B. Li, K. Kumar, I. Roy, A. V. Morozov, O. V. Emelyanova, L. Zhang, T. Koc, S. Belin, J. Cabana, R. Dedryvere, A. M. Abakumov, J. M. Tarascon, *Nat. Mater.* **2022**, *21*, 1165.

[16] N. Sun, Y. Song, Q. Liu, W. Zhao, F. Zhang, L. Ren, M. Chen, Z. Zhou, Z. Xu, S. Lou, F. Kong, J. Wang, Y. Tong, J. Wang, *Adv. Energy Mater.* **2022**, *12*, 2200682.

[17] N. Wu, P. H. Chien, Y. Qian, Y. Li, H. Xu, N. S. Grundish, B. Xu, H. Jin, Y. Y. Hu, G. Yu, J. B. Goodenough, *Angew. Chem., Int. Ed. Engl.* **2020**, *59*, 4131.

[18] a) S. Tan, Z. Shadike, J. Li, X. Wang, Y. Yang, R. Lin, A. Cresce, J. Hu, A. Hunt, I. Waluyo, L. Ma, F. Monaco, P. Cloetens, J. Xiao, Y. Liu, X.-Q. Yang, K. Xu, E. Hu, *Nat. Energy* **2022**, *7*, 484; b) T. Liu, L. Yu, J. Liu, J. Lu, X. Bi, A. Dai, M. Li, M. Li, Z. Hu, L. Ma, D. Luo, J. Zheng, T. Wu, Y. Ren, J. Wen, F. Pan, K. Amine, *Nat. Energy* **2021**, *6*, 277.

[19] Y. Xiao, K. Turcheniuk, A. Narla, A. Y. Song, X. Ren, A. Magasinski, A. Jain, S. Huang, H. Lee, G. Yushin, *Nat. Mater.* **2021**, *20*, 984.

[20] J. Ma, Z. Liu, B. Chen, L. Wang, L. Yue, H. Liu, J. Zhang, Z. Liu, G. Cui, *J. Electrochem. Soc.* **2017**, *164*, A3454.

[21] a) Q. S. Liu, H. W. An, X. F. Wang, F. P. Kong, Y. C. Sun, Y. X. Gong, S. F. Lou, Y. F. Shi, N. Sun, B. Deng, J. Wang, J. J. Wang, *Natl. Sci. Rev.* **2023**, *10*, nwac272; b) Z. Xiong, Z. Wang, W. Zhou, Q. Liu, J.-F. Wu, T.-H. Liu, C. Xu, J. Liu, *Energy Storage Mater.* **2023**, *57*, 171.